Dynamical analysis of a satellite-observed anticyclonic eddy in the northern Gulf of Anadyr of the Bering Sea

4 authors, including:

Yineng Li
Chinese Academy of Sciences
15 PUBLICATIONS 37 CITATIONS

Xiaofeng Li
NOAA/NESDIS
173 PUBLICATIONS 1,545 CITATIONS

Jia Wang
National Oceanic and Atmospheric Administra…
121 PUBLICATIONS 2,012 CITATIONS

RESEARCH ARTICLE

Key Points:
- An anticyclonic eddy was detected by SAR, SST, and ocean color images in 21 April 1999
- The barotropic instability is the main energy source for the growth of the eddy
- The dynamical reasons for the asymmetric structure of the eddy are investigated

Correspondence to:
S. Peng,
speng@scsio.ac.cn

Dynamical analysis of a satellite-observed anticyclonic eddy in the northern Gulf of Anadyr of the Bering Sea

Yineng Li[1], Xiaofeng Li[2], Jia Wang[3], and Shiqiu Peng[1,4]

[1]State Key Laboratory of Tropical Oceanography, South China Sea Institute of Oceanology, Chinese Academy of Sciences, Guangzhou, China, [2]GST at NOAA/NESDIS, College Park, Maryland, USA, [3]NOAA Great Lakes Environmental Research Laboratory, Ann Arbor, Michigan, USA, [4]School of Oceanography, Qinzhou University, Qinzhou, China

Abstract The characteristics and evolution of a satellite-observed anticyclonic eddy in the northern Gulf of Anadyr (northwestern Bering Sea) during March and April 1999 are investigated using a three-dimensional Princeton Ocean Model (POM). The anticyclonic-like current pattern and asymmetric feature of the eddy were clearly seen in the synthetic aperture radar (SAR), sea surface temperature, and ocean color images in April 1999. The results from model simulation reveal the three-dimensional structure of the anticyclonic eddy, its movement, and dissipation. Energy analysis indicates that the barotropic instability (BTI) is the main energy source for the growth of the anticyclonic eddy. The momentum analysis further reveals that the larger magnitude of the barotropic pressure gradient in the meridional direction causes the asymmetry of the anticyclonic eddy in the zonal and meridional directions, while the different magnitudes of the meridional baroclinic pressure gradient are responsible for the different intensity of currents between the northern and southern parts of the anticyclonic eddy.

1. Introduction

The Bering Sea is a high-latitude, semienclosed sea with an extensive continental shelf in the east, and a narrow continental shelf to the west. Like many subarctic seas, the Bering Sea is characterized by seasonal extremes between winter and summer temperatures. Primary production at the shelf break of the Bering Sea starts rising in spring and increases throughout summer when eddies develop and play a significant role in changing the biogeochemistry of the upper ocean [*McGillicuddy et al.*, 1998; *Oschlies and Garcon*, 1998; *Oschlies*, 2002; *Williams and Follows*, 2003]. Previous studies showed high chlorophyll-*a* (Chl-*a*) distributions are associated with mesoscale eddies in the Bering Sea [*Sapozhnikov*, 1993; *Mizobata et al.*, 2002; *Mizobata and Saitoh*, 2004; *Okkonen et al.*, 2004]. The region of high primary production in the "Green Belt" (the shelf break of Bering Sea) roughly coincides with the region of high eddy variability and the eddy-induced, on-shelf flux of nutrients can enhance primary production from spring to summer at the shelf break [*Mizobata et al.*, 2008].

Previous modeling studies have investigated the impact of eddies or oceanic processes on the biogeochemistry in the Bering Sea [*Clement et al.*, 2005; *Maslowski et al.*, 2008; *Clement et al.*, 2009; *Hu and Wang*, 2010]. Collectively, the results suggest that mesoscale eddies play a decisive role in the exchange of properties between the northern Bering Sea shelf and the southern Bering Sea basin. In addition, *Wang and Ikeda* [1997] and *Zhang et al.* [2011] confirm the importance of mesoscale instabilities along sloping topography and their ability to strongly affect local large-scale circulation along the Bering Sea shelf break. A model study by *Kinney et al.* [2009] examined the relationship between the Bering Sea currents and on-shelf property fluxes. They found that canyons along the shelf break appear to be more prone to eddy activity than regions without canyons. These eddy activities occur in the shelf break of the central or eastern Bering Sea and induce higher rates of on-shelf transport. However, to our knowledge, documentation and investigations of eddy activities in the region of the northwestern Bering Sea are extremely rare, particularly for the large and relatively steady eddies in the Gulf of Anadyr (Figure 1) during the spring or summer. Thus, it is interesting and necessary to investigate the characteristics and evolution of eddies in this region.

In this paper, satellite remote sensing data, including synthetic aperture radar (SAR) images, ocean color and sea surface temperature (SST) data, and model simulation outputs, are employed to demonstrate the
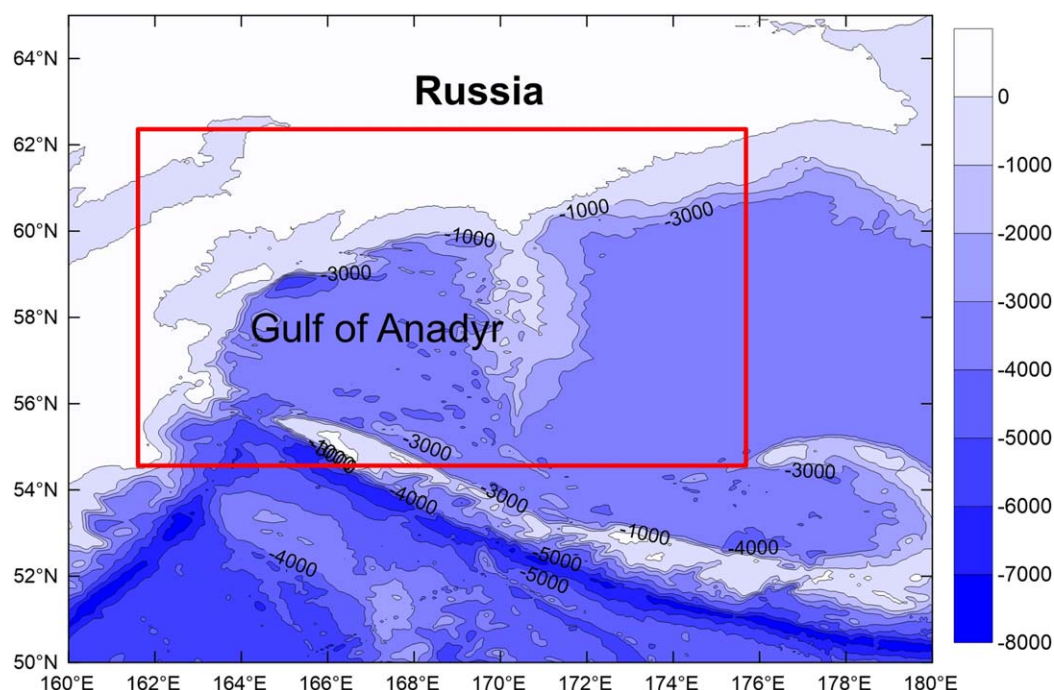
Figure 1. (a) Bathymetry (unit: m) and the model domain (the red Box).

three-dimensional characteristics and evolution of an anticyclonic eddy that occurred in the northern Gulf of Anadyr in spring 1999. The surface features of the eddy from satellite observations are given in section 2. The characteristics and evolution of the eddy from model simulation are shown in section 3. Section 4 presents the energy and momentum analysis to explore the potential mechanisms of eddy generation and growth. Section 5 gives a summary.

2. Surface Features of the Anticyclonic Eddy From Satellite Observations

The satellite data used in this study include a C-band RADARSAT-1 synthetic aperture radar (SAR) image, 4 km resolution reanalysis sea-surface temperature (SST) from the Advanced Very High Resolution Radiometer (AVHRR), and 4 km resolution chlorophyll a (Chl-*a*) concentration from MODIS-Aqua and 1/3 $\times$ 1/3° gridded sea-level anomaly (SLA) data from AVISO (Archiving, Validation and Interpretation of Satellite Oceanographic data).

Figure 2 shows the climatologically monthly mean Chl-*a* concentration in the Gulf of Anadyr in spring (March–May) from 2002 to 2014. It is obvious that the concentration of Chl-*a* is gradually increasing from March to May. In April, a relatively low Chl-*a* concentration area in the northern Gulf of Anadyr (indicated by the black box in Figure2b) is surrounded by higher Chl-*a* concentration water. Such a low Chl-*a* concentration area is coincident with higher climatological SLA observations from AVISO (Figure 2d). Both of the above data sets suggest a steady and strong anticyclonic eddy with a horizontal scale of over 100 km occurring in the northern Gulf of Anadyr in spring for some years. This anticyclonic eddy can be further confirmed by the anticyclonic-like current pattern from the SAR image and the warm surface water center from AVHRR SST anomaly on 18 April 1999 (Figures 3a and 3b). SAR is an active microwave radar that provides high-resolution (10–100 m) ocean surface imagery under all weather conditions, day and night. Ocean phenomena that interact with the active microwave radar pluses will modulate the radar backscatter signal, and thus, allowing them to appear as distinguished features in these images [*Li et al.*, 2002, 2008, 2009]. Figure 3a is a RADARSAT-1 scanSAR mode SAR image with a swath width of 450 km and a spatial resolution of 150 m. The coincidence of the anticyclonic current pattern with the positive SST anomaly implies the features of an anticyclonic eddy, i.e., clockwise-rotation and convergence of surface water within the eddy.
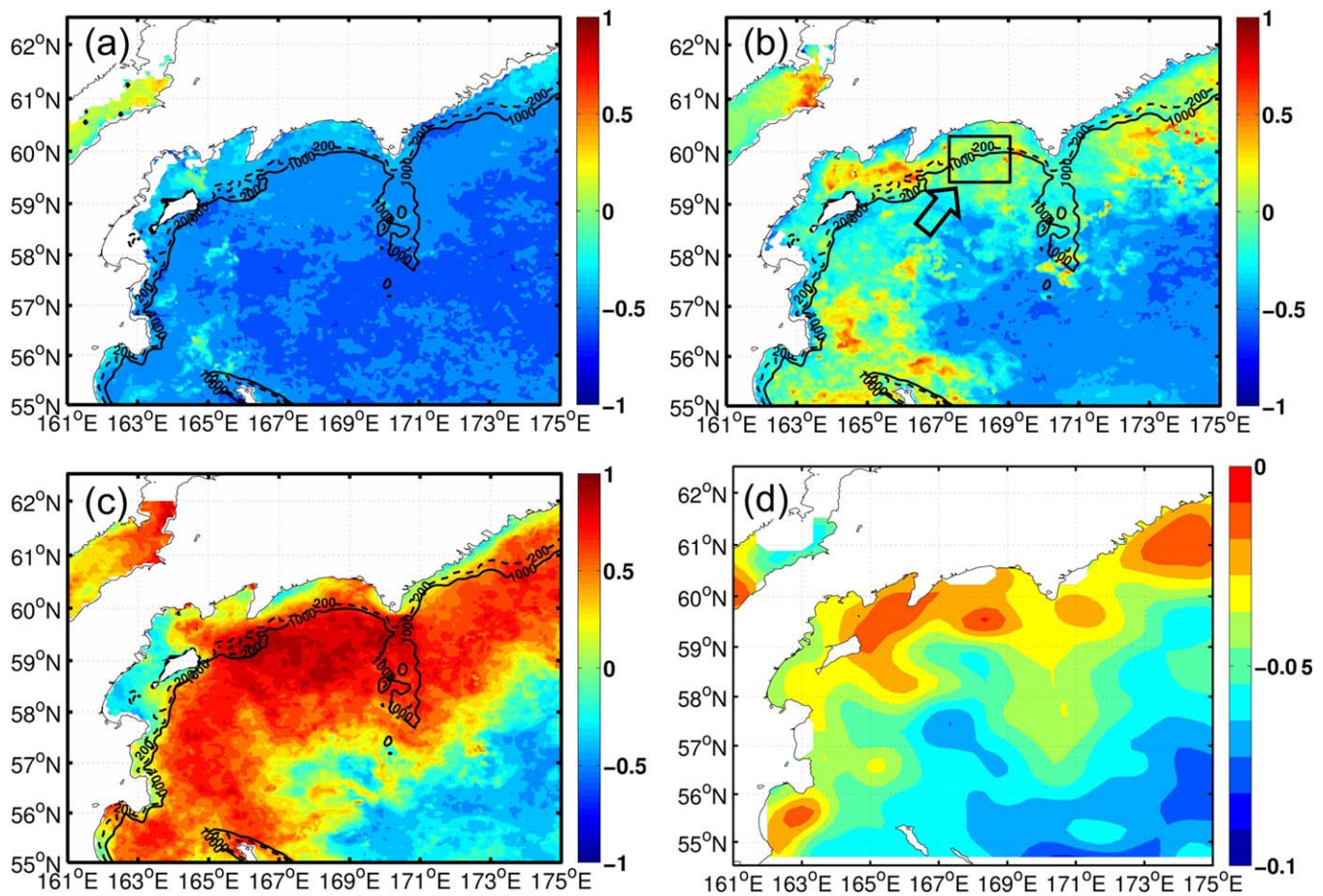
Figure 2. The climatologically monthly-mean log-scaling Chl-*a* concentration (unit: log(mg m^{-3})) in the Gulf of Anadyr from MODIS data in (a) March; (b) April; (c) May during 2002–2014 (the black-dashed and solid lines are the 200 and 1000 m isobaths, respectively); and (d) climatologically monthly-mean sea level anomaly (SLA, unit: m) in April from AVISO data.

3. Three-Dimensional Characteristics and Evolution of the Anticyclonic Eddy From Model Simulation

The SAR, SLA, and low Chl-*a* concentration maps reveal the existence of the anticyclonic eddy in the northern Gulf of Anadyr in the northwestern Bering Sea with a horizontal scale of over 100 km. However, these
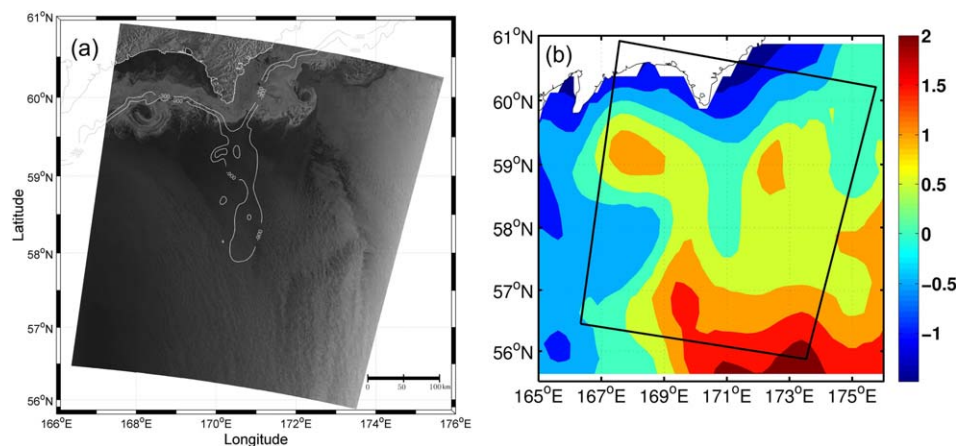

Figure 3. (a) The current pattern from the RADARSAT-1 ScanSAR image acquired at 19:00Z on 18 April 1999 (the white lines are the 300 and 900 m isobaths, respectively) and (b) the AVHRR SST anomaly (unit: °C) on the same day as the SAR image.

satellite-based observations only provide the surface features of the eddy and it is our goal in this paper to use high-resolution model outputs from the Princeton Ocean Model (POM) to analyze the three-dimensional structure and energy of the eddy.

3.1. Model Configuration

The 2002 version of the POM [*Blumberg and Mellor*, 1987; *Mellor*, 2004] is employed in this study. The POM is a 3-D, fully nonlinear, primitive equation ocean model, with the 2.5 order turbulence closure scheme of *Mellor and Yamada* [1982] for calculating turbulence viscosity and diffusivity.

The model domain (Figure 1) is from 54.6°N to 62.4°N and 161.4°E to 175.7°E, with a horizontal resolution of 0.04° (about 2.3–4.5km) and 23 vertical layers in sigma coordinate refined in the upper ocean. The Bering Sea has a Rossby radius of deformation of 12–20 km according to *Chelton et al.* [1998], thus the horizontal grid in our model allows us to resolve most of the mesoscale eddies in the region. The one-arc-minute global relief model of Earth's topography and bathymetry (ETOPO1) [*Marks and Smith*, 2006] is used. For the nearshore region, the model's minimum depth is set to 10 m, based on a physical stability criterion of the global stability by *Wang* [1996]: $h_{min} + \zeta_{max} > 0$ where h_{min} is the minimum water depth and ζ_{max} is the maximum water elevation possibly caused by strong (gusty) winds along the coast. The external and internal time steps are set to 6 and 240 s, respectively. Monthly mean data from the Simple Ocean Data Assimilation (SODA) reanalysis [*Carton et al.*, 2000a, 2000b] are used for the open boundaries of the domain. The normal advection of different variables at the open boundaries is governed by the radiation boundary condition [*Mellor*, 2004].

The initialization procedure of the ocean model includes two steps. First, the POM is integrated from a rest state of the ocean (i.e., "cold start"). The initial temperature and salinity are from the climatological fields of the World Ocean Atlas 2001 (WOA01) for January [*Boyer et al.*, 2002], and the climatological monthly mean wind stress, heat flux, and shortwave radiation flux are from the National Center for Atmospheric Research (NCAR)/National Center of Environment Prediction (NCEP) reanalysis [*Kalnay et al.*, 1996]. After a spin-up of 10 model years, the upper ocean can reach a quasi-equilibrium state [*Zhang and Qian*, 1999]. The second step is to integrate the POM from 1 January 1998 to 31 December 2010. The daily meteorological forcing data, including sea surface winds, air temperature, humidity, E-P (Evaporation minus Precipitation), and shortwave radiation flux are obtained from the NCEP/NCAR reanalysis as well. The tides are incorporated into the model through the open boundaries with 13 tidal constituents from the OTPS (Oregen State University Tidal Prediction Software) [*Egbert et al.*, 1994].

3.2. Model Validation

To see how well the model simulates ocean interior fields, we validate the model results against the Argo profiles available in the model region. Argo profiles of 146 are collected from the products in the USGODAE (US Global Ocean Data Assimilation Experiment, http://www.usgodae.org) in the area of Figure 4a [160°E~177°°E; 54°N~62°N] in March, April, and May (MAM) during 2003–2010. The RMSEs of modeled temperature and salinity against Argo profiles are calculated as follows:

$$RMSE = \sqrt{\frac{1}{N}\sum_{i=1}^{N}(x_i - y_i)^2}, \tag{1}$$

where x_i and y_i ($i = 1, 2, 3 \ldots N$) are the modeled and observed samples of any variable such as temperature. N is the total sampling number. As shown in Figure 4b, the maximum RMSEs of temperature and salinity are 0.5°C and 0.2 psu, respectively, both of which locate in the thermocline layer (~200–300m). The larger RMSEs of temperature in the thermocline are probably due to the bias of heat flux calculation which does not include effect of the sea ice concentration. On the whole, the RMSEs of modeled temperature and salinity are relatively small with a vertical mean of 0.3°C and 0.13psu, respectively. Therefore, the model simulation results are reliable and thus can be used for further analysis.

3.3. Three-Dimensional Characteristics and Evolution of the Eddy

Figures 5 and 6 show the monthly mean current anomalies (vectors), SLA, and the SSTA (SST anomaly) (with respect to the 12 year mean for 1999–2010) from the model outputs for April 1999. An anticyclonic vortex is clearly found in the northern Gulf of Anadyr in the northwestern Bering Sea with clockwise anomalous
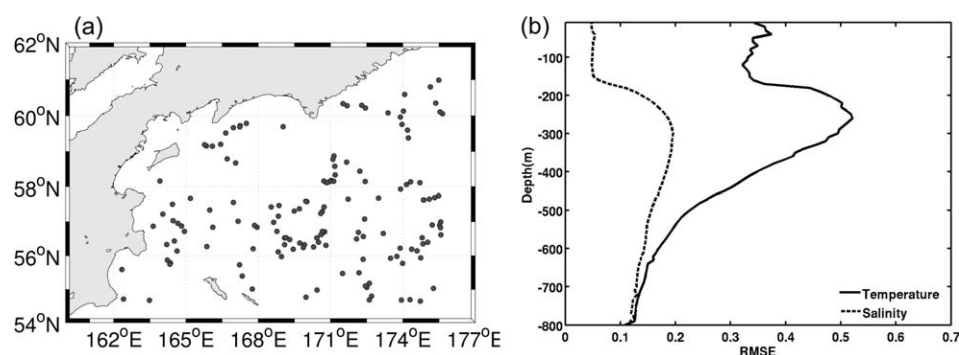
Figure 4. (a) Locations of the Argos in March, April, and May (MAM) during 2003–2010; the RMSEs of modeled (b) temperature (unit: °C) and salinity (unit: psu) against Argo data in MAM during 2003–2010.

currents (Figures 5a and 6) and positive SLA and SSTA (as indicated by the black box in Figures 5a and 5b). The locations of these anomalies are approximately in the same area as those observed by satellite observations (Figures 2d and 3). The flow of the northern branch of the eddy follows the arc-like isobaths of 500–2000m in the northern Gulf of Anadyr, suggesting a link between the eddy and the Anadyr currents flowing along the 500–2000 m isobaths. The magnitude of the current anomalies reaches a maximum of over 0.2 m/s around 150–300m depth and decreases gradually with depth (Figure 6). The asymmetric feature of the anticylonic eddy can be clearly seen in different magnitudes of current anomalies in both horizontal and vertical directions. The zonal current anomalies (especially the positive anomalies in the northern part of the eddy) shown in the meridional section (Figure 6a) are much larger and deeper than the meridional current anomalies shown in the zonal section (Figure 6b). For the zonal current anomalies, the eastward velocity (in the northern part of the eddy) is stronger than the westward velocity (in the southern part of the eddy), with the former extending to 1700 m (Figure 6a) and the later only to 1200 m (with respect to anomaly magnitude >0.1 m/s). For the meridional current anomalies, however, the northward velocity (in the western part of the eddy) is comparable to the southward velocity (in the eastern part of the eddy), and both are limited to the upper 800–1000 m depth (Figure 6b). In addition, contours of density anomalies in the meridional section are leaning, while those in the zonal section are relatively flat. The spatial difference of the vertical depth of the anticyclonic eddy current anomalies may be due to the difference of the barotropic and/or baroclinic pressure gradients. The deep penetration of the anticyclonic eddy could have a significant impact on the water exchange between the shelf and the deep basin, which could further influence the local biogeochemistry processes. Thus, further investigation into the evolution of the eddy as well as the related energy transformation would prove valuable.

To see the temporal evolution of the eddy, we plot the current anomalies every 10 or 11 days with respect to the 3 month mean from 11 March to 21 May 1999 (Figure 7). It can be seen that the anticyclonic eddy was formed in March near 169.2°E, 59°N with a diameter of about 50 km (Figure 7b). At that time, the main
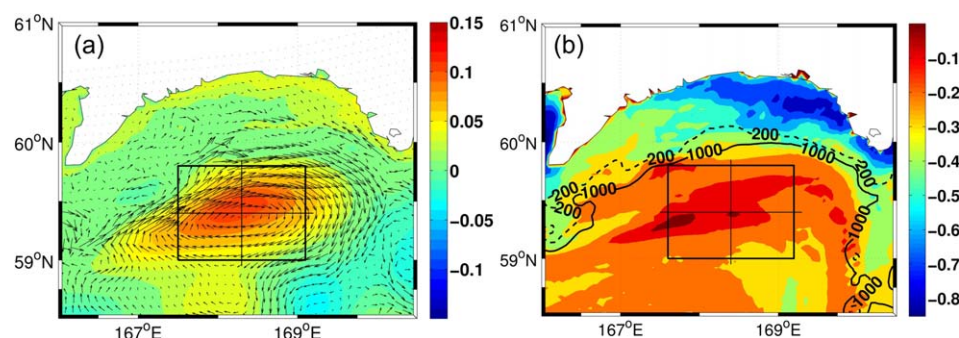

Figure 5. Monthly mean current vectors (a) anomaly superimposed with SLA and (b) the SSTA (with respect to the 12 year mean of 1999–2010) of April from the model outputs (the black box and cross sections are referred to in other figures, the black-dashed and solid lines are the 200 and 1000 m isobaths, respectively).
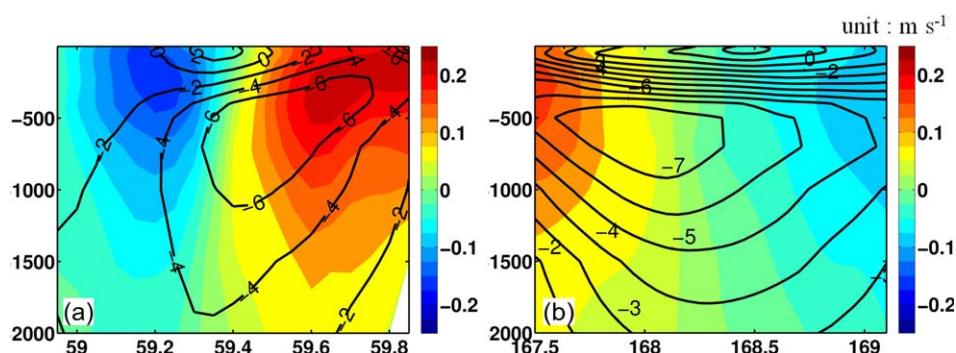
Figure 6. Anomalies of density (contours: kg m^{-3}) and normal velocity (shadings; m s^{-1}) from model output averaged during April, along the (a) meridional and (b) zonal sections (indicated in Figure 5) across the eddy.

circulation along the 500–2000 m isobaths was strong. In early April, the anticyclonic eddy moved northward to the location near 169.3°E, 59.3°N with an enlarged horizontal scale and enhanced intensity (Figures 7c and 7d). By late April, the anticyclonic eddy moved westward to the location near 168.3°E, 59.4°N (Figure 7e). Previous studies in the other regions of the Bering Sea also found that mesoscale eddies, which penetrate to depths of at least 1000 m [_Roden_, 1995; _Mizobata et al._, 2002; _Johnson et al._, 2004], propagate northwestward along the shelf break [_Okkonen_, 2001; _Mizobata and Saitoh_, 2004]. The anticyclonic eddy was well developed with a diameter of about 100 km in the zonal direction, twice that of the eddy in March. The southwestward current anomalies along the 500–2000m isobaths changed to northeastward/eastward (Figures 7e and 7f). Finally, the anticyclonic eddy dissipated in May (Figure 7h).

The periodical change of speed of currents in the northern Gulf of Anadyr was in pace with the strength change of the northeasterly winds from March to May 1999 (Figures 7 and 8). In March (Figure 8a), the wind stress was quite strong compared to April and May (Figures 8b and 8c). In April, the wind stress greatly decreased, and the preexisting southwestward currents were gradually weakened or even reversed (Figures 7c, 7d, and 8b). These changes facilitated the relaxation of the pressure gradient formed in March with the strong wind stress and were favorable for the formation of an anticyclonic eddy. At the "dissipating" stage in May, the winds continued to relax (Figure 8c), which resulted in the reverse of the current anomalies shown in the early March (Figures 7f and 7g). During the whole evolution process, the anticyclonic eddy moved northwestward from March to April and dissipated in May. The relation between the growth of the anticyclonic eddy and the Anadyr currents can be further confirmed by a linear solution of the stability equation for the wave growth based on the idealized zonal Anadyr currents, which suggests that it is the relaxation or instability of the Anadyr current along the 500–2000 m isobaths during April that leads to a positive growth rate of the anticyclonic eddy (Appendix A).

To further investigate the effect of wind variation on the eddy generation and growth, an additional experiment is performed besides the aforementioned experiment (denoted as "CTRL"). The additional experiment is the same as "CTRL" except that the wind field is fixed since 15 March 1999 (denoted as "FIXED"). The results are shown in Figure 9. An anticyclonic current and higher SLA can be seen in the "CTRL" run (Figure 5a), but no apparent eddy with SLA over 0.04 m is found in FIXED (Figure 9). The results indicate that the relaxation of wind field in spring 1999 is the main factor for the generation and growth of the anticyclonic eddy.

4. Energy and Momentum Analysis

Previous studies suggested that instabilities in the mean flow, wind forcing, and topographic interactions are the important factors for eddy generation mechanisms [e.g., _Mizobata et al._, 2008; _Paluszkiewicz and Niebauer_, 1984; _Schumacher and Stabeno_, 1994]. As shown in section 3.2, the evolution of the anticyclonic eddy is highly associated with the variation of the strength of wind stress and the Anadyr current (Figures 7–9, Appendix A), suggesting a potential mechanism for the generation and growth of the eddy. In this section, we will examine the relative contributions from the wind stress work and the current-induced barotropic and baroclinic energy transfer to the eddy energy variation during the evolution of the anticyclonic eddy.
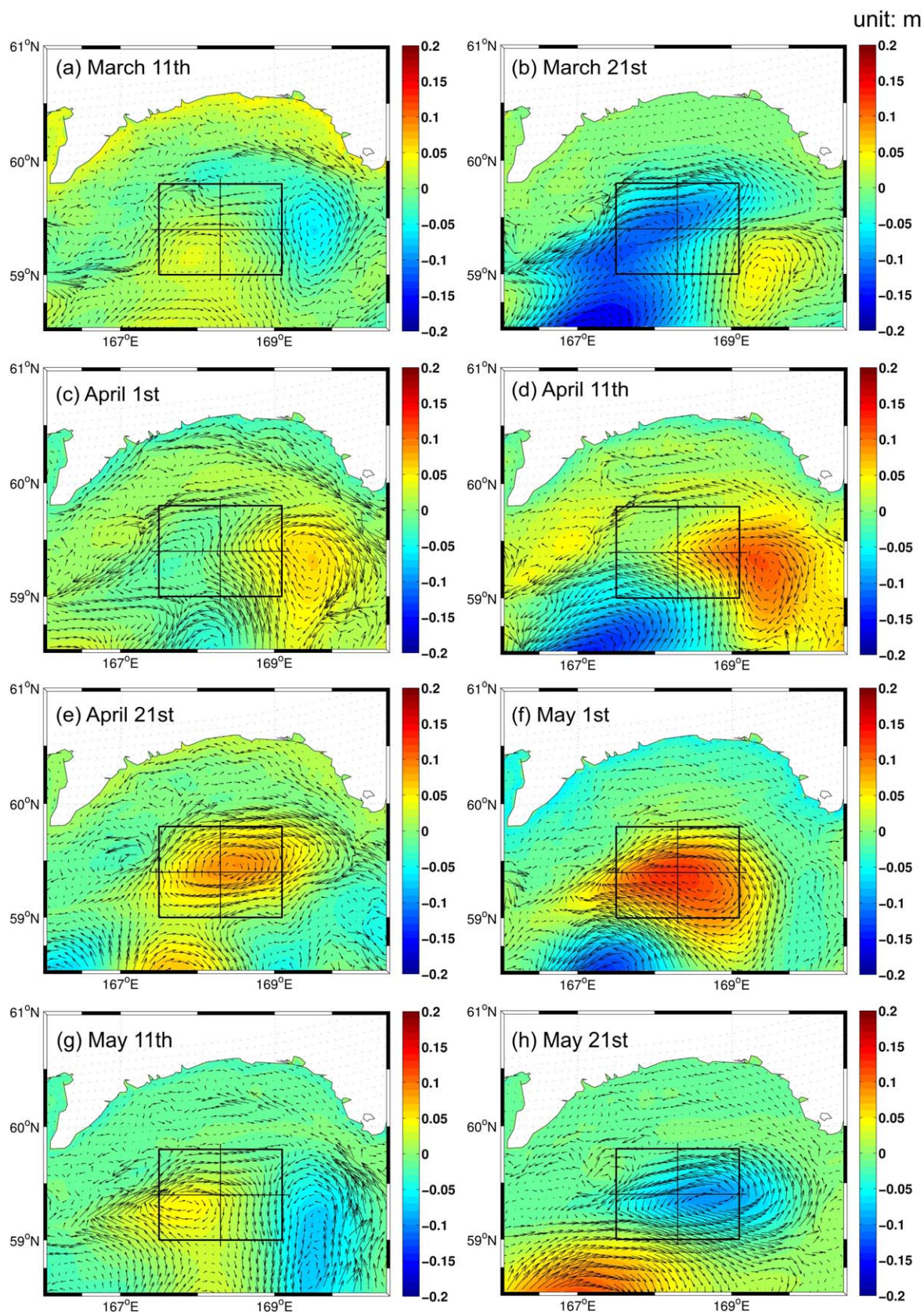
Figure 7. The monthly mean current anomaly pattern (vectors) superimposed with SLA (shadings, unit: m) of (a) 11 March; (b) 21 March; (c) 1 April; (d) 11 April; (e) 21 April; (f) 1 May; (g) 11 May, and (h) 21 May with respect to the 3 -monthly mean from March to May 1999.
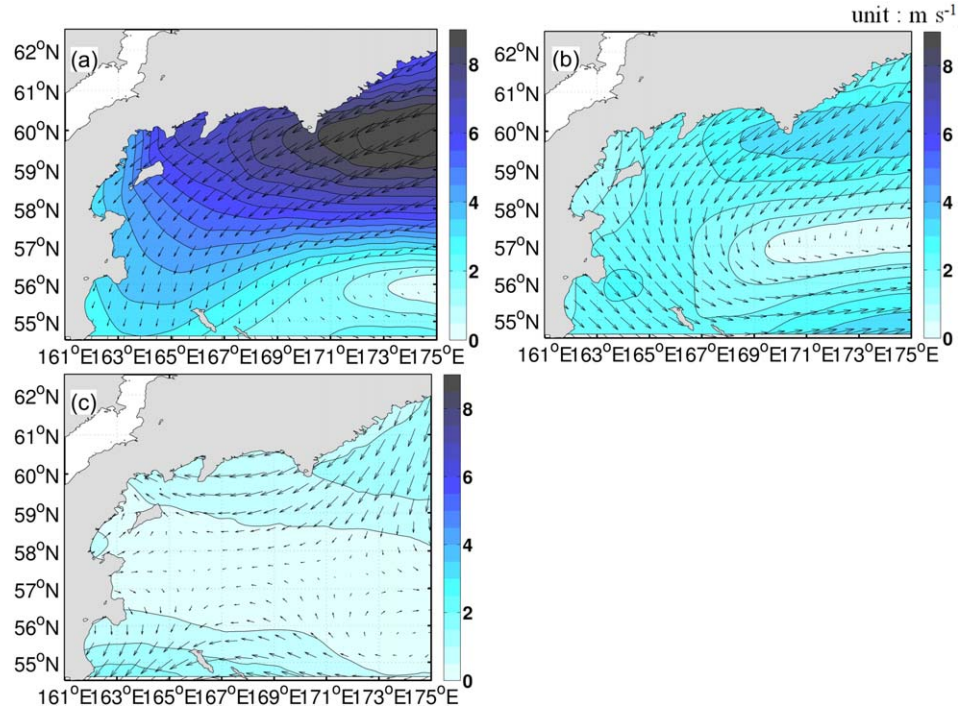
Figure 8. Vectors and velocity (shadings, unit: m s^{-1}) of monthly wind at 10 m in (a) March; (b) April; and (c) May from NCEP reanalysis.

4.1. Energy Transfer Induced by Current Instability

Eddy-related energy could be calculated from the model output to quantitatively estimate the contributions from various mechanisms during the development of the anticyclonic eddy. Eddy kinetic energy (EKE) and eddy available potential energy (EPE) per unit mass are defined as [*Böning and Budich*, 1992]:

$$EKE = \frac{1}{2}\left(u'^2 + v'^2\right) \tag{2}$$

$$EPE = -\frac{g\tilde{\rho}'^2}{2\rho(\mathrm{d}\rho_\theta(z)/\mathrm{d}z)} \tag{3}$$

in which g is gravitational acceleration, $\tilde{\rho}(x,y,z,t) = \rho(x,y,z,t) - \rho_0(z)$ with $\rho_0(z)$ is a depth-dependent background density and temporally averaged from March to May, and $\rho_\theta(z)$ is the potential density of the background state. Prime denotes the deviation from the mean state that is averaged from March to May in 1999, i.e., $u = \bar{u} + u'$, $v = \bar{v} + v'$, $\rho = \bar{\rho} + \rho'$, where the overbar denotes the time average from March to May.

The energy transfer between the mean and eddy potential energy or between the mean and eddy kinetic energy could be illustrated by the four-box energy diagram [*Lorenz*, 1955; *Böning and Budich*, 1992; *Beck-mann et al.*, 1994]. Some insight into instability mechanisms can be gained by considering energy transfer from mean to eddy energy. Following *Böning and Budich* [1992], *Brown and Fedorov* [2010], and *Zu et al.* [2013], the interactions between eddy and mean flow are defined as:

$$T2 = -\frac{g}{\rho(d\rho_\theta(z)/dz)}\left(u'\tilde{\rho}'\frac{\partial\bar{\tilde{\rho}}}{\partial x} + v'\rho'\frac{\partial\bar{\tilde{\rho}}}{\partial y}\right) \tag{4}$$

and

$$T4 = -\left(u'u'\frac{\partial\bar{u}}{\partial x} + u'v'\left(\frac{\partial\bar{v}}{\partial x} + \frac{\partial\bar{u}}{\partial y}\right) + v'v'\frac{\partial\bar{v}}{\partial y}\right), \tag{5}$$

where $T2$ represents the conversion between the mean potential energy (MPE) and EPE, and $T4$ is the work of the Reynolds stress against the mean shear, namely, the conversion between mean kinetic energy (MKE)
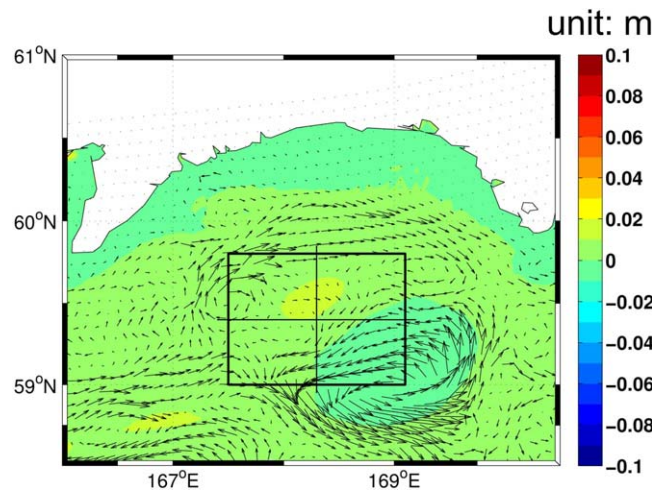
Figure 9. The same as Figure 5a except for the experiment FIXED.

and EKE. A positive value of $T2$ indicates a baroclinic instability (BCI), while a positive value of $T4$ indicates a barotropic instability (BTI).

Figures 10a and 10b show the horizontal distributions of vertically integrated (upon 400 m) EKE and EPE averaged during April. An energetic region is found in the northern Gulf of Anadyr, especially with respect to the EKE. Similar to the pattern of current anomalies (Figure 7), the EKE is high along the 59.8°N latitude (in the shelf slope of ∼500–2000 m isobaths) and around 59.2°N latitude (in the basin with depth of ∼3000 m), indicating an asymmetrical feature of EKE distribution. The vertical integrations of $T4$ and $T2$ in the upper 400 m also show strong BTI and BCI in the area where the anticyclonic eddy located, suggesting that large energy is transferred from the mean flow to the eddy. In general, the magnitude of BTI is much larger than that of BCI in the area where the anticyclonic eddy is located, implying that the BTI process is more important for the growth of the anticyclonic eddy. The enhanced BCI in this area is probably caused by the density difference between the shelf break water and deep ocean water. The strengthened BTI is probably due to the variation of the Anadyr current and the strong large-scale wind stress (Figure 8) that changes the velocity shear of the upper layer currents, as schematically illustrated in Figure 11.

4.2. The Energy Budget Analysis

Energy budget analysis can provide insights on the generation and growth of an eddy. Besides the BTI and BCI induced by a pressure gradient discussed previously, the variation of the EKE is balanced by terms of
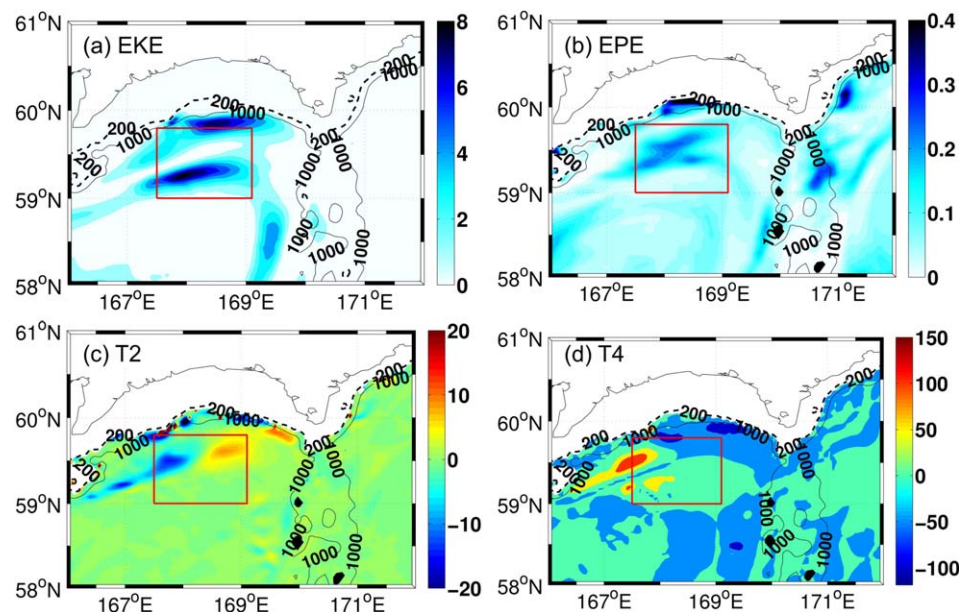

Figure 10. Horizontal distribution of vertical integrated monthly mean (a) EKE; (b) EPE; (c) T2; and (d) T4 (unit: m² s⁻²) in the upper 400m averaged during April. The black box shows the average location of the anticyclonic eddy (the black dashed and solid lines are the 200 and 1000 m isobaths, respectively).
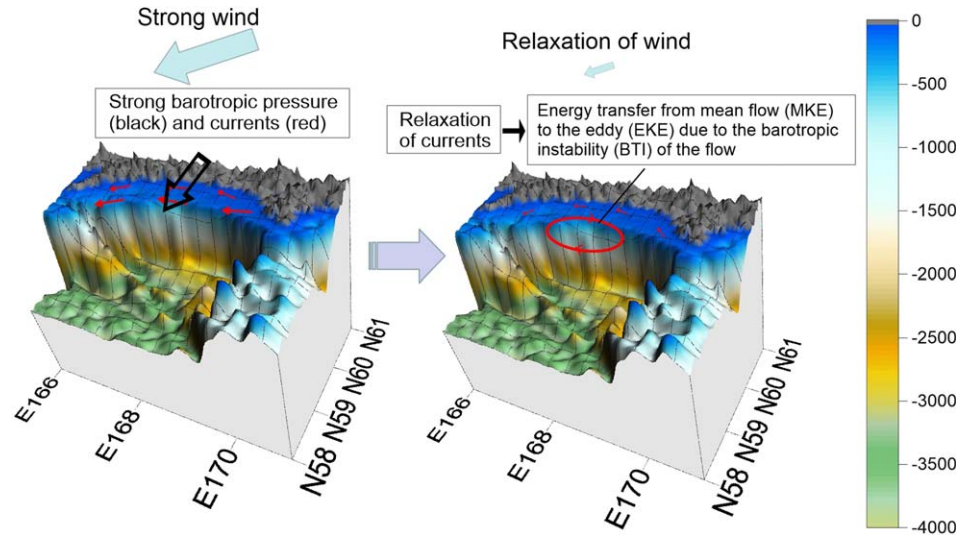
Figure 11. Cartoon of the energy transformation through relaxation of wind and currents, the bathymetry (unit: m) is shown by the 3-D surface.

wind stress work, Coriolis force work, advection of EKE, and friction work. Here, we employ the following vertically integrated momentum equations [*Mellor*, 2004]:

$$\frac{\partial uD}{\partial t} = -\underbrace{\frac{\partial u^2 D}{\partial x} - \frac{\partial uvD}{\partial y} + \tilde{F}_x + G_x}_{AD} + \underbrace{fvD}_{COR} - \underbrace{gD\frac{\partial \eta}{\partial x}}_{PBT}$$

$$-\underbrace{\frac{gD}{\rho_0}\int_{-1}^{0}\int_{\sigma}^{0}\left[D\frac{\partial \rho'}{\partial x} - \frac{\partial D}{\partial x}\sigma'\frac{\partial \rho'}{\partial \sigma}\right]d\sigma'd\sigma}_{PBC} - \underbrace{\langle wu(0)\rangle}_{WS} + \underbrace{\langle wu(-1)\rangle}_{BOT} \tag{6}$$

and

$$\frac{\partial vD}{\partial t} = -\underbrace{\frac{\partial v^2 D}{\partial y} - \frac{\partial uvD}{\partial x} + \tilde{F}_y + G_y}_{AD} - \underbrace{fuD}_{COR} - \underbrace{gD\frac{\partial \eta}{\partial y}}_{PBT}$$

$$-\underbrace{\frac{gD}{\rho_0}\int_{-1}^{0}\int_{\sigma}^{0}\left[D\frac{\partial \rho'}{\partial y} - \frac{\partial D}{\partial y}\sigma'\frac{\partial \rho'}{\partial \sigma}\right]d\sigma'd\sigma}_{PBC} - \underbrace{\langle wv(0)\rangle}_{WS} + \underbrace{\langle wv(-1)\rangle}_{BOT}, \tag{7}$$

where x, y, and z are the conventional Cartesian coordinates; g is the sea level; $D = H + \eta$ is the total water depth, with $H (x, y)$ being the bottom topography and $\eta(x, y, t)$ the surface elevation; σ is the sigma coordinate ranging from $\sigma = 0$ at the sea surface to $\sigma = -1$ at the bottom; ρ and ρ' are the density and density perturbation, respectively. Terms 1–6 on the right hand side of equations (6) and (7) are referred to nonlinear advection and diffusion (AD), Coriolis force (COR), barotropic pressure gradient (PBT), baroclinic pressure gradient (PBC), bottom friction stress (BOT), and surface wind stress (WS). To calculate the EKE defined by equation (2), we rewrote equations (6) and (7) in the form of perturbation:

$$\left(\frac{\partial uD}{\partial t}\right)' = AD'_u + COR'_u + PBT'_u + PBC'_u + WS'_u + BOT'_u, \tag{8}$$

$$\left(\frac{\partial vD}{\partial t}\right)' = AD'_v + COR'_v + PBT'_v + PBC'_v + WS'_v + BOT'_v, \tag{9}$$

where the prime denotes the deviation from the mean state of March–May in 1999. Then the approximate EKE tendency equation can be obtained by a combination of equations (8) and (9), i.e., $(u' \cdot (8) + v' \cdot (9))/D$, which leads to

$$
\begin{aligned}
\frac{\partial EKE}{\partial t} &= \underbrace{(u' \cdot AD'_u + v' \cdot AD'_v}_{WAD} + \underbrace{u' \cdot COR'_u + v' \cdot COR'_v}_{WCOR} \\
&\quad + \underbrace{u' \cdot PBT'_u + v' \cdot PBT'_v}_{WPBT} + \underbrace{u' \cdot PBC'_u + v' \cdot PBC'_v}_{WPBC} \\
&\quad + \underbrace{u' \cdot WS'_u + v' \cdot WS'_v}_{WWS} + \underbrace{u' \cdot BOT'_u + v' \cdot BOT'_v}_{WBOT})/D
\end{aligned}
\tag{10}
$$

Terms in equation (10) are referred to as the works of advection and diffusion (WAD), Coriolis force (WCOR), pressure gradient, wind stress (WWS), and bottom friction (WBOT). The work of pressure gradient consists of two parts: barotropic and baroclinic pressure gradients (WPBT and WPBC). It should be noted that the WWS defined here is the "direct" wind effect on the EKE. Total wind stress work could be divided into the two parts that are associated with MKE and EKE, respectively; the wind stress work on the mean flow does not directly affect EKE, but through other processes such as BTI. The increased horizontal or vertical shears of the mean current induced by winds might lead to the growth of instability and the transfer of MKE into EKE through the $T4$ term. The time-series of each term in equation (9) are shown in Figure 12, which are area-averaged within the black box in Figure 5 and vertically integrated. There are two peaks of positive EKE tendency in April (i.e., 31–60 days), suggesting the development of the eddy with increasing total EKE. It is obvious that the contribution of WPBT (the green line in Figure 12) to the increase of EKE dominates among all other terms. This fact implies that the growth of the eddy is mainly due to transfer of MKE to EKE through the BTI mechanism, i.e., the changes of Anadyr current and wind stress. The effect of the "direct" wind forcing on the EKE (WWS) is seen in the first peak of EKE increase, but is much smaller than the effect of WPBT. In contrast, the role of WPBC acts to restrict the growth of the eddy with its magnitude comparable to that of WPBT; negative values of WPBC suggest a dissipation of EKE through baroclinic processes. The other terms such as the WBOT have limited contributions to the EKE as their magnitudes are much smaller. Therefore, the WPBT associated with the BTI is the main factor of the anticyclonic eddy growth in the northern Gulf of Anadyr.
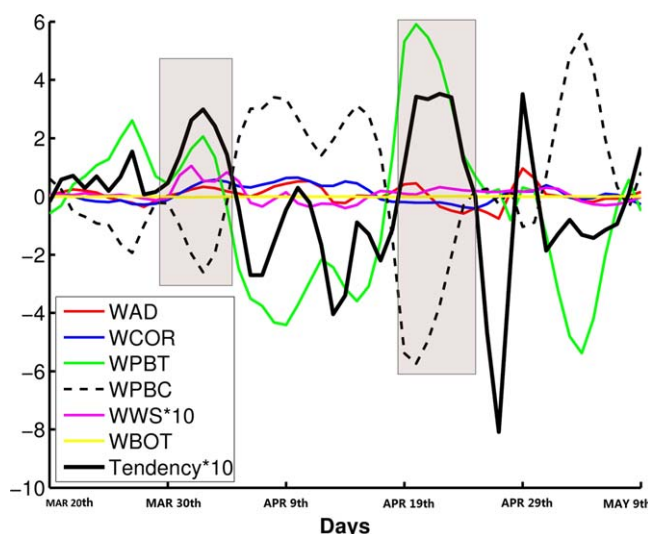

Figure 12. The time series of each energy term anomalies and the residue of all the terms (units: $m^3 \, s^{-2}$) averaged over the anticyclonic eddy area (the black box indicated in Figure 5). The wind stress work term and the residue have been amplified 10 times for visibility.

4.3. The Momentum Budget Analysis of the Anticyclonic Eddy

Momentum budget analysis can explain the elliptic structure of the anticyclonic eddy, i.e., why the zonal velocity of the eddy is stronger than the meridional velocity. Terms in equations (5) and (6) are normalized by D (the total water depth) in this study. The momentum budgets in the zonal direction along 59.4°N and meridional direction along 168.3°E (indicated in Figure 5) are shown in Table 1. In the zonal direction, positive (negative) values of the COR represent northward (southward) current anomalies. In the meridional direction, positive (negative) values of the COR represent the westward (eastward) current anomalies. It can be seen that the COR is mainly balanced by the pressure

Table 1. The 30 Day Mean Momentum Term Anomalies (units: m^3 s^{-2}) of the Four Parts of the Anticyclonic Eddy in the Zonal and Meridional Momentum Equations in April

	Zonal Section		Meridional Section	
	West	East	South	North
AD	3.13	−0.89	4.43	7.24
COR	36.05	−45.18	73.96	−127.85
PBT	−72.73	65.75	−150.22	154.54
PBC	35.14	−19.56	71.18	−33.21
WS	0.19	0.26	0.10	0.13
BOT	0.07	0.04	0.02	0.23

gradient terms PBT and PBC. Therefore, the eddy circulation is primarily dominated by the geostrophic balance as schematically shown in Figure 13. The residual of the geostrophic balance is one order of magnitude smaller than the COR and pressure gradient. The values of the PBT are the largest among all the terms, indicating that the barotropic pressure gradient is the control factor of the balance. This is consistent with the early discussion that BTI is the main energy source of the anticyclonic eddy. Moreover, the values of the PBT in the meridional section are larger than those in the zonal section; this could be the main cause of the asymmetry of the currents of the anticyclonic eddy in the two directions. It is also interesting to note the asymmetry of the current intensity in the meridional section, i.e., the magnitudes of the zonal velocities in the northern part of the meridional section (eastward currents) are much larger than those in the southern part (westward currents) (also see Figure 6a). This is probably due to differences in the PBC magnitudes. As shown in Table 1 and Figure 13, the geostrophic balance is between the PBT and COR + PBC (i.e., COR+PBC≈-PBT). Since the magnitudes of the PBT are comparable and the COR has the same sign as the PBC, the smaller magnitude of the PBC in the northern part of the meridional section results in the larger magnitude of the COR (larger eastward current) compared to that in southern part.

5. Conclusions

An anticyclonic eddy in the northern Gulf of Anadyr was detected by a SAR and satellite SST images on 18 April 1999. This eddy can also be identified in the climatological surface Chl-*a* and SLA maps in April, with a horizontal scale of over 100 km and an asymmetrical shape. The POM model is able to simulate the asymmetrical structure and evolution of the anticyclonic eddy. Both the model simulation and climatological surface Chl-*a* show tha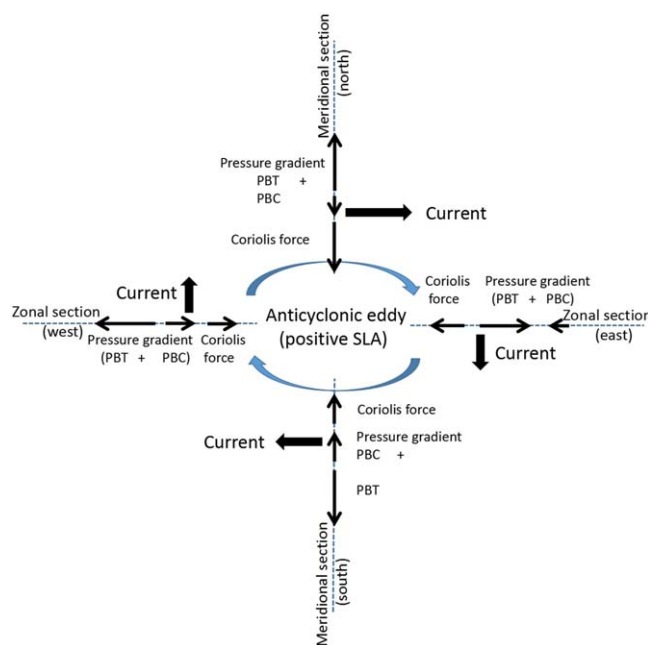t the anticyclonic eddy was generated in March, moved northwest and matured in April, and finally dissipated in May. Sensitive experiments and energy analysis reveals that the relaxations of the pressure gradient and currents formed in March along with a strong wind stress play a significant role in the energy conversion from MKE to EKE (the barotropic instability), and that the work of the barotropic pressure gradient associated with the barotropic instability is the main factor of the growth of the anticyclonic eddy. The momentum analysis reveals that the larger barotropic pressure gradient in the meridional direction results in the asymmetry of the anticyclonic eddy in the zonal and meridional directions. In addition, the different magnitudes of the meridional baroclinic pressure gradient are responsible for the different intensity of flows between the northern and southern parts of the
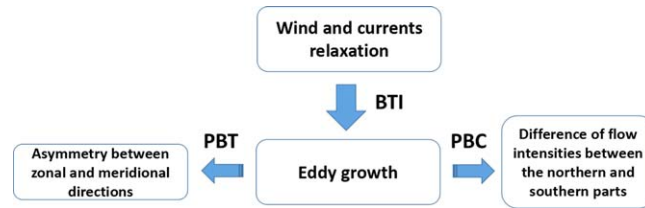

Figure 13. A sketch of geostrophic balance of the anticyclonic eddy with 30 day mean momentum term anomalies (Pressure gradient = Barotropic pressure gradient + Baroclinic pressure gradient, units: m^3 s^{-2}).

Figure 14. Schematic diagram illustrating the mechanisms of eddy growth and formation of the asymmetric structure. BTI denote the barotropic instability, PBT denote the barotropic pressure gradient, and PBC denote the baroclinic pressure gradient.

anticyclonic eddy. The mechanism and dynamical processes of the anticyclonic eddy are schematically illustrated in Figure 14. Furthermore, the anticyclonic eddy found in this study may have impact on the biogeochemistry processes in the region, which can be investigated using a biogeochemistry-physics coupled model in our future work.

Appendix A: A Linear Solution for the Wave Growth Due to the Instability of Basic Flow

As discussed in section 3, the anticyclonic eddy is associated with the mean flow of the Anadyr currents flowing along the 500–2000 m isobaths. The relationship between eddy growth and basic flow can be explained by the linear and nonlinear solutions of the barotropic and baroclinic instabilities radiated from a jet [*Pedlosky*, 1993; *Kamenkovich and Pedlosky*, 1996, 1998a, 1998b; *Hristova* et al. 2008; *Wang et al.*, 2013]. Generally, the instability problem can be addressed by a simple barotropic quasi-geostrophic model, which is described by the barotropic vorticity equation:

$$\frac{\partial \zeta}{\partial t} + J(\psi, q) = F \text{ and } \zeta = \nabla^2 \psi + \beta y \qquad (A1)$$

where ψ is stream function, ζ potential vorticity, F an external forcing and friction, J the Jacobian operator, and β the Coriolis parameter.

To simplify the problem, let us consider a basic state with a parallel zonal western boundary current $\bar{u}(y)$. We set x = 0 at the center of the Gulf of Anadyr currents, and x = $-L_x/2$ or $L_x/2$ (L_x = 200km in this study) at the boundary where the current speed is assumed to be zero. The linearized equation (A1) becomes

$$\left(\frac{\partial}{\partial t} + \bar{u} \frac{\partial}{\partial x}\right) \nabla^2 \psi + \beta^* \psi_y - \bar{u}_{yy} \psi_x - F(\psi) = 0, \qquad (A2)$$

where $\beta^* = \beta L_b^2 / U$ is the nondimensional beta, and $F(\psi)$ is the frictional damping on perturbations, which is neglected for the linear simulation. A normal mode solution is assumed in *x* and *t* for perturbation:

$$\psi = \phi(x) e^{ik(x-ct)}, \qquad (A3)$$

where $k = 2\pi n / L_x$ is zonal wavenumber, c is zonal phase speed. Substituting equation (A3) into (A2) results in a Sturm-Liouville eigenvalue problem,

$$\phi_{yy} + \frac{\beta^*}{ik(\bar{u} - c)} \phi_y - \left(k^2 \frac{\bar{u}_{yy}}{\bar{u} - c}\right) = 0, \qquad (A4)$$

This is the stability equation for an inviscid, barotropic, and quasi-geostophic zonal current. Previous studies either further simplified it to an ordinary differential equation system by choosing a step function or a continues profile to represent the boundary current $\bar{u}$. In this study, the model outputs from POM along 500–2000 m isobaths in the black
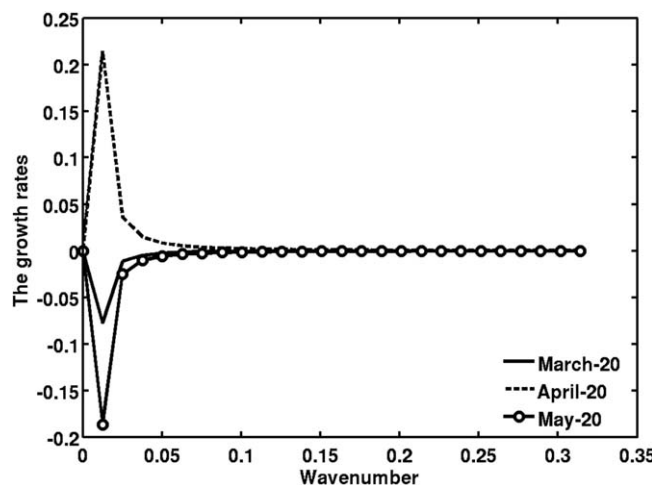

Figure A1. (a) The growth rates (ω_i) as a function of wavenumber *k* and (b) the imaginary along with the real part of ω on 20 March, 20 April, and 20 May.

box indicated in Figure 5a are used for the current and stream function estimate, from which we can solve the time dependent relationship between wavenumber and phase speed. The imaginary part ω_i of c represents the linear growth rate which is a function of wavenumber k ($\omega_i = kci$), with a positive value of ω_i indicating the wave (or eddy) growth due to instability of the basic flow. As shown in Figure A1 the growth rate on 20 April is positive but negative on 20 March and 20 May, suggesting that the relaxation or instability of the Anadyr current along the 500–2000 m isobaths during April leads to a growth of the anticyclonic eddy. The linear growth rate is larger at smaller wavenumbers, indicating those waves with larger wavelength $\lambda = 2\pi/k$ are easier to be radiated ($\lambda > 200$ km in this study).

References

Beckmann, A., C. W. Böning, B. Brügge, and D. Stammer (1994), On the generation and role of eddy variability in the central North Atlantic Ocean. *J. Geophys. Res.*, 99(C10), 20,381–20,391.

Blumberg, A. F., and G. L. Mellor (1987), A description of a three-dimensional coastal ocean circulation model, in *Three-Dimensional Coastal Ocean Models*, edited by N. S. Heaps, pp. 1–16, AGU, Washington, D. C.

Böning, C. W., and R. G. Budich (1992), Eddy dynamics in a primitive equation model: Sensitivity to horizontal resolution and friction, *J. Phys. Oceanogr.*, 22(4), 361–381.

Boyer, T. P., C. Stephens, J. I. Antonov, M. E. Conkright, R. A. Locarnini, T. D. O'Brien, and H. E. Garcia (2002), in *World Ocean Atlas 2001: Salinity. NOAA Atlas NESDIS 50*, edited by S. Levitus, pp. 176–182, U.S. Gov. Print. Off., Washington, D. C.

Brown, J. N., and A. V. Fedorov (2010), How much energy is transferred from winds to the thermocline on ENSO time scales?, *J. Clim.*, 23, 1563–1579.

Carton, J. A., G. Chepurin, X. Cao, and B. Giese (2000a), A simple ocean data assimilation analysis of the global upper ocean 1950-1995 Part I: Methodology, *J. Phys. Oceanogr.*, 30, 294–309.

Carton, J. A., G. Chepurin, and X. Cao (2000b), A simple ocean data assimilation analysis of the global upper ocean 1950-1995 Part II: Results, *J. Phys. Oceanogr.*, 30, 311–326.

Chelton, D. B., R. A. DeSzoeke, M. G. Schlax, K. E. Naggar, and N. Siwertz (1998), Geographical variability of the first baroclinic Rossby radius of deformation. *J. Phys. Oceanogr.*, 28, 433–460.

Clement, J. L., W. Maslowski, L. W. Cooper, J. M. Grebmeier, and W. Walczowski (2005), Ocean circulation and exchanges through the northern Bering Sea19792001: Model results, *Deep Sea Res., Part II*, 52(17), 3509–3540.

Clement, K. J., W. Maslowski, and S. R. Okkonnen (2009), On the processes controlling shelf-basin exchange and outer shelf dynamics in the Bering Sea, *Deep Sea Res., Part II*, 56(17), 1351–1376.

Egbert, G. D., A. F. Bennett, and M. G. G. Foreman (1994), TOPEX/Poseidon tides estimated using a global inverse model, *J. Geophys. Res.*, 99(C12), 24,821–24,852.

Hristova, H. G., J. Pedlosky, and M. A. Spall (2008), Radiating instability of a meridional boundary current, *J. Phys. Oceanogr.*, 38(10), 2294–2307.

Hu, H., and J. Wang (2010), Modeling effects of tidal and wave mixing on circulation and thermohaline structures in the Bering Sea: Process studies, *J. Geophys Res.*, 115, C01006, doi:10.1029/2008JC005175.

Johnson, G. C., P. J. Stabeno, and S. C. Riser (2004), The Bering Slope Current system revisited, *J. Phys. Oceanogr.*, 34, 384–398.

Kalnay, E, et al. (1996), The NCEP/NCAR 40-year reanalysis project, *Bull, Am. Meteorol. Soc.*, 77(3), 437–471, doi:10.1175/1520-0477(1996)077.

Kamenkovich, I. V., and J. Pedlosky (1996), Radiating instability of nonzonal ocean currents, *J. Phys. Oceanogr.*, 26, 622–643.

Kamenkovich, I. V., and J. Pedlosky (1998a), Radiation of energy from nonzonal ocean currents, nonlinear regime. Part I: Single wave development. *J. Phys. Oceanogr.*, 28, 1683–1701.

Kamenkovich, I. V., and J. Pedlosky (1998b), Radiation of energy from nonzonal ocean currents, nonlinear regime. Part II: Interactions between waves, *J. Phys. Oceanogr.*, 28, 1683–1701.

Kinney, J. C., W. Maslowski, and S. Okkonen (2009), On the processes controlling shelf basin exchange and outer shelf dynamics in the Bering Sea, *Deep Sea Res., Part II*, 56, 1351–1362, doi:10.1016/j.dsr2.2008.10.023.

Li, X., W. Pichel, M. He, S. Wu, K. Friedman, P. Clemente-Colon, and C. Zhao (2002), Observation of hurricane-generated ocean swell refraction at the Gulf Stream North Wall with the RADARSAT-1 synthetic aperture radar, *IEEE Trans. Geosci. Remote Sens.*, 40(10), 2131–2142, doi:10.1109/TGRS.2002.802474.

Li, X., Z. Zhao, and W. Pichel (2008), Internal solitary waves in the northwestern South China Sea inferred from satellite images, *Geophys. Res. Lett.*, 35, L13605, doi:10.1029/2008GL034272.

Li, X., C. Li, Q. Xu, and Pichel W. (2009), Sea surface manifestation of along-tidal-channel underwater ridges imaged by SAR, *IEEE Trans. Geosci. Remote Sens.*, 47(8), 2467–2477, doi:10.1109/TGRS.2009.2014154.

Lorenz, E. N. (1955), Available potential energy and the maintenance of the general circulation, *Tellus*, 7(2), 157–167.

Marks, K. M., and W. H. F. Smith (2006), An evaluation of publicity available global bathymetry grids, *Mar. Geophys. Res.*, 27, 19–34.

Maslowski, W., R. Roman, and J. C. Kinney (2008), Effects of mesoscale eddies on the flow of the Alaskan Stream, *J. Geophys. Res.*, 113, C07036, doi:10.1029/2007JC004341.

McGillicuddy, D. J., A. R. Robinson, D. A. Siegel, H. W. Jannasch, R. Johnson, T. Dickeys, J. McNeil, A. F. Michaels, and A. H. Knap (1998), Influence of mesoscale eddies on new production in the Sargasso Sea, *Nature*, 394(6690), 263–266.

Mellor, G. L. (2004), *Users Guide for a Three-Dimensional, Primitive Equation, Numerical Ocean Model (June 2004 version)*, 53 pp., Program in Atmos. and Oceanic Sci., Princeton Univ, Princeton, N. J.

Mellor, G. L., and T. Yamada (1982), Development of a turbulence closure model for geophysical fluid problems, *Rev. Geophys. Space Phys.*, 20, 851–875.

Mizobata, K., and S. Saitoh (2004), Variability of Bering Sea eddies and primary productivity along the shelf edge during 1998–2000 using satellite multisensory remote sensing, *J. Mar. Syst.*, 50, 101–111.

Mizobata, K., S. I. Saitoh, A. Shiomoto, T. Miyamura, N. Shiga, K. Imai, M. Toratani, Y. Kajiwara, and K. Sasaoka, (2002), Bering Sea cyclonic and anticyclonic eddies observed during summer 2000 and 2001, *Prog. Oceanogr.*, 55, 65–75.

Mizobata, K., S.-I. Saitoh, and J. Wang (2008), Interannual variability of summer biochemical enhancement in relation to mesoscale eddies at the shelf break in the vicinity of the Pribilof Islands Bering Sea, *Deep Sea Res., Part II*, 55, 1717–1728.

Okkonen, S. R. (2001), Altimeter observations of the Bering Slope current eddy field, *J. Geophys. Res., 106*(C2), 2465–2476.

Okkonen, S. R., G. M. Schmidt, E.D. Cokelet, and P. J. Stabeno (2004), Satellite and hydrographic observations of the Bering Sea 'Green Belt'. *Deep Sea Res., Part II, 51*, 1033–1051.

Oschlies, A. (2002), Can eddies make ocean deserts bloom?, *Global Biogeochem. Cycles, 16*(4), 1106, doi:10.1029/2001GB001830.

Oschlies, A., and V. Garcon, (1998), Eddy-induced enhancement of primary production in a model of the North Atlantic Ocean, *Nature, 394*, 266–269.

Paluszkiewicz, T., and H. J. Niebauer (1984), Satellite observations of circulation in the Eastern Bering Sea, *J. Geophys. Res., 89*(C3), 3663–3678, doi:10.1029/JC089iC03p03663.

Pedlosky, J. (1993), The reflection of unstable baroclinic waves and the production of mean coastal currents. *J. Phys. Oceanogr., 23*, 2130–2135.

Roden, G. I. (1995), Aleutian Basin of the Bering Sea: Thermohaline, oxygen, nutrient, and current structure in July 1993, *J. Geophys. Res., 100*(C7), 13,539–13,554, doi:10.1029/95JC01291.

Sapozhnikov, V. V. (1993), Influence of mesoscale anticyclonic eddies on the formation of hydrochemical structures in the Bering Sea, *Oceanology [English Transl.], 33*, 299–304.

Schumacher, J. D., and P. J. Stabeno (1994), Ubiquitous eddies of the eastern Bering Sea and their coincidence with concentrations of larval pollock, *Fish. Oceanogr., 3*, 182–190.

Wang, J. (1996), Global linear stability of the 2-D shallow water equations: An application of the distributive theorem of roots for polynomials on the unit circle, *Mon. Weather Rev., 24*(6), 1301–1310.

Wang, J., and M. Ikeda (1997), Diagnosing ocean unstable baroclinic waves and meanders using the quasigeostrophic equations and the Q-vector method, *J. Phys. Oceanogr., 27*, 1158–1172.

Wang J. B., A. S. Michael, R. F. Glenn, and M. R. Paola (2013), Nonlinear Radiating instability of a barotropic eastern boundary current, *J. Phys. Oceanogr., 43*(7), 1439–1452.

Williams, R. G., and M. J. Follows (2003), Physical transport of nutrients and the maintenance of biological production, in *Ocean Biogeochemistry; The Role of the Ocean Carbon Cycle in Global Change, IGBP Series*., edited by M. J. R. Fasham, Springer, Berlin.

Zhang Y., J. Pedlosky, and G. R. Flierl (2011), Cross-shelf and out-of-bay transport driven by an open-ocean current, *J. Phys. Oceanogr., 41*, 2168–2185.

Zhang, Y. C., and Y. F. Qian (1999), Numerical simulation of the regional ocean circulation in the coastal area of China, *Adv. Atmos. Sci., 16*(3), 443–450.

Zu, T. T., D. X. Wang, C. X. Yan, I. Belkin, W. Zhuang, and J. Chen (2013), Evolution of an anticyclonic eddy southwest of Taiwan, *Ocean Dyn., 63*(5), 519–531.